*J Mater Sci: Mater Electron* (2022) 33:11498–11510

# Room-temperature chemiresistive g-$C_3N_4$/$Ag_2ZrO_3$ nanocomposite gas sensor for ethanol detection

S. P. Subin David[1], S. Veeralakshmi[1], M. Sakthi Priya[2], S. Nehru[3,*], and S. Kalaiselvam[1,*]

[1] Department of Applied Science and Technology, A.C. Tech. Campus, Anna University, Chennai, Tamil Nadu 600025, India
[2] Department of Materials and Mineral Resources Engineering, National Taipei University of Technology, No. 1, Section 3, Chung – Hsiao East Road, Taipei 106, Taiwan
[3] Department of Physical Chemistry, University of Madras, Guindy Campus, Chennai, Tamil Nadu 600025, India

**Received:** 24 September 2021
**Accepted:** 17 March 2022
**Published online:** 6 April 2022



## ABSTRACT

Designing the efficient ethanol gas sensors with high sensitivity, selectivity, and stability is of great interest in diverse applications. Herein, g-$C_3N_4$, $Ag_2ZrO_3$, and g-$C_3N_4$/$Ag_2ZrO_3$-based nanomaterials have been synthesized, characterized, and subjected for gas sensor studies against 50 ppm concentration of six different gases namely n-butanol, isopropanol, methanol, xylene, toluene, and ethanol at room temperature. All nanomaterials g-$C_3N_4$, $Ag_2ZrO_3$, and g-$C_3N_4$/$Ag_2ZrO_3$ have shown higher response values of 15.1, 24.5, and 53.1%, respectively, against ethanol gas compared to other gases. The observation of highest response value of g-$C_3N_4$/$Ag_2ZrO_3$ may be due to involvement of cooperative effect of g-$C_3N_4$ and $Ag_2ZrO_3$ in the nanocomposite. Further, the elaborated gas sensor studies of g-$C_3N_4$/$Ag_2ZrO_3$ showed that the present nanocomposite material has excellent repeatability, quick response/recovery, and good stability for the detection of ethanol gas. By careful modification of this kind of semiconductor, metal oxide-based nanocomposites will afford room-temperature-operatable high-performance ethanol gas sensors in near future.

## 1 Introduction

Ethanol is intensely penetrated into our day today life as one of the volatile organic compounds (VOCs). It is extensively used for medical treatment, alcoholic drinks, food industry, and industrial chemistry process. However, it is important to monitor that long-term exposure of excess ethanol to humans can cause severe injuries for instance irritation of eyes and skin, coma, and even intoxication which threaten lives [1–4]. Thus, it is extremely needed to build up a highly selective as well as sensitive ethanol gas sensor to prevent potential injuries caused by ethanol. Further, ethanol gas sensors can be used in various applications such as monitoring industrial ethanol gas leakage, measuring the ethanol concentration in the blood by means of breath alcohol checker using the exhaled ethanol gas of human breath, etc. Even

Address correspondence to E-mail: nehruchem@gmail.com; kalai@annauniv.edu


https://doi.org/10.1007/s10854-022-08124-w

there have been different approaches that are available for ethanol gas sensing, it is still a great interest to develop chemiresistive-type alternative materials for ethanol gas sensors. Particularly, semiconducting metal oxide-based gas sensors have been greatly paying attention due to their high sensitivity, long-term stability, simple fabrication, and low cost [5–8].

Importantly, the performance of semiconducting metal oxides-based gas sensors is typically reliant on the device working temperature, due to the operating temperature that has an imperative part in controlling the conductivity, electron mobility, and kinetics of surface reactions. In general, conventional metal oxide-based gas sensors are needed higher temperatures like in the range of 150–500 °C for their operation. This minimum thermal energy is required for the gas-sensing measurement to defeat the activation energy barrier in the surface redox reaction of metal oxide and also used to enlarge the free carrier concentration in the metal oxides. Further, the usage of higher operational temperature makes reducing its limits for broader applications by lowering sensor stability, possibility of risks by the explosive and flammable gases, and device energy consumption. Thus, it is also needed to develop alternative materials for the efficient room-temperature operatable ethanol gas sensor applications [9–11].

Even there have been a diversity of metal oxides such as $WO_3$ [12], $TiO_2$ [13, 14], $In_2O_3$ [15, 16], ZnO [17–19], $SnO_2$ [20, 21], etc. are available for ethanol gas-sensing applications, studies on the room-temperature operatable ethanol gas sensor materials are limited in the literature. Hence, a rational designing of materials are needed for attaining highly selective as well as sensitive ethanol gas sensors. There are several strategies available for enhancing the sensitivity and selectivity of semiconducting metal oxides for ethanol gas-sensing applications. It includes incorporation of noble metals [22, 23], preparation of binary/ternary metal oxides composites [24, 25], and synthesis of different morphological nanostructures [26–28]. Porous nanomaterials are often used as gas-sensing materials and its structural parameters like grain size, grain agglomeration, pore size, and surface morphology are playing important role in the sensor performance [29, 30]. Among the many strategies used, developing composite materials using metal oxides and graphitic structure materials have been showed very good results for tailoring the sensitivity and selectivity of gas sensors.

Recent days, researchers have been attracted with graphitic carbon nitride (g-$C_3N_4$) due to its numerous advantages like high chemical stability, large specific surface area, easy preparation, and non-toxicity. Further, its medium band gap offers pathway to modulate its electronic structure via doping or chemical functionalization. This kind of tuning the electronic structure is a potential factor in optimizing gas sensor properties [31]. Numerous studies pointing on g-$C_3N_4$-loaded different metal oxide composites have been resulted that g-$C_3N_4$ plays a very vital role in the activity of composites. The g-$C_3N_4$ nanosheets can offer several grown sites for other semiconducting substrates, which can improve the charge transport and limit the recombination possibility of charge carriers. Hence, g-$C_3N_4$ nanosheets ought to be a potential material for the gas-sensing applications [32]. Even there are few reports that are available for the g-$C_3N_4$-based ethanol gas sensors, still it is needed to improve the performance of the nanomaterials in terms of sensitivity, selectivity, operational temperature, and stability for the commercial applications [33, 34]. Thus, the present work was aimed to investigate the impact of g-$C_3N_4$/$Ag_2$-$ZrO_3$-based nanocomposite for sensing some of the VOCs at room temperature. As this nanocomposite has shown higher ethanol gas-sensing behavior, the material was further subjected to detailed ethanol gas sensor studies to measure the sensor response, sensor efficiency, sensitivity, repeatability, and stability against the different concentrations.

## 2 Experimental section

### 2.1 Materials and methods

Melamine (Sigma-Aldrich 99% purity), zirconyl chloride octahydrate ($ZrOCl_2.8H_2O$, 99.9% Merck) and silver nitrate (99.9% Merck) were used for synthesis of nanomaterials. All other chemicals were of analytical grade and double-distilled water was used throughout the investigations. All calibrated gases were obtained from Chemix special gases and equipments, India. The XRD analysis for the prepared nanomaterials was conducted by X-ray diffractometry (D2 Phaser, Bruker). UV–visible diffuse reflectance spectra (UV–Vis DRS) were recorded in the wavelength range of 200–800 nm using a Perkin Elmer, Lambda 850 UV/Vis spectrophotometer

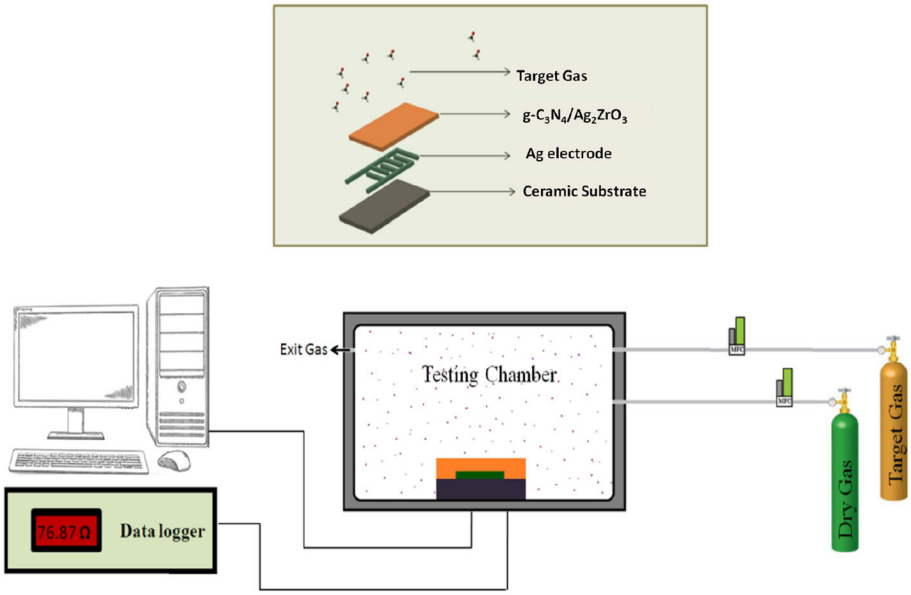


**Fig. 1** Pictorial representation of gas sensor set-up

equipped with an integrating sphere accessory using $BaSO_4$ as the reference. JEOL JSM-7610F instrument was used to obtain Field emission scanning electron microscopy (FE-SEM) images of the samples. Transmission electron microscopy (TEM) images were taken with a Hitachi H7650 electron microscope. Surface area of nanomaterials was taken for about 10 mg of the sample for each analysis (Quantachrome Chem BET-3000 analyzer). The gas sensor studies were performed by adopting the same experimental procedure as reported in our previous paper and pictorial representation of gas sensor set-up is shown in Fig. 1 [35].

## 2.2 Synthesis of graphitic carbon nitride

g-$C_3N_4$ was synthesized based on the previous reported procedure [36]. In brief, calcination of melamine (5.0 g) at 550 °C for 4 h under the heating rate of 3.5 °C/min in a high-temperature muffle furnace resulted to yield a yellow solid, which was pulverized into powder, and washed with excess amount of water and ethanol. The obtained sample was further subjected to dry at 80 °C for 12 h, followed by kept to store in a vacuum desiccator.

## 2.3 Synthesis of $Ag_2ZrO_3$

$Ag_2ZrO_3$ was synthesized by following reported procedure [37]. In brief, 100 mL aqueous solution of zirconyl chloride octahydrate (0.355 g) was ultrasonicated for 30 min, and then 0.071 g $AgNO_3$ was added followed by ultrasonicated for 30 min. Then, the resulted precipitate was washed with excess amount of water and ethanol and was dried for overnight at room temperature. The obtained sample was kept to store in a vacuum desiccator.

## 2.4 Synthesis of g-$C_3N_4$/$Ag_2ZrO_3$ composite (1:1 weight ratio)

To synthesis g-$C_3N_4$/$Ag_2ZrO_3$ composite, 0.355 g of $Ag_2ZrO_3$ in 100 mL of water was dispersed by ultrasonication for 30 min, and then 0.355 g of g-$C_3N_4$ was added in the above solution and continued to ultrasonicate for 30 min. The resultant precipitate was washed with excess amount of water and ethanol and was dried for overnight at room temperature. The product was collected and stored in the vacuum desiccator [38].

# 3 Results and discussion

## 3.1 Structural and surface morphological analysis

The crystalline nature and phase purity of g-$C_3N_4$, $Ag_2ZrO_3$, and g-$C_3N_4$/$Ag_2ZrO_3$ were analyzed using X-ray diffraction pattern (XRD). A peak at 27.5° in the XRD pattern of g-$C_3N_4$ (JCPDS: 87-1526) belongs to (002) planes of the interlayer stacking of aromatic

components and tris-triazine units of g-$C_3N_4$, which have been also noted in the g-$C_3N_4$/$Ag_2ZrO_3$ nanocomposite [39, 40]. All the diffraction peaks of $Ag_2ZrO_3$ perfectly match with that of previously reported $Ag_2ZrO_3$ and which corresponds to 2$\theta$ values of 27.85°, 32.25°, 46.25°, 54.80°, 57.50°, 67.50°, 74.51°, and 77.10°. The crystalline phases of $Ag_2ZrO_3$ are compared and resulted in similar with $Na_2ZrO_3$ and $Ag_2SnO_3$, because the structural chemistry of $Ag_2ZrO_3$ is not well studied in the literature [41–43]. Further, it is also noted that the characteristic peak positions of g-$C_3N_4$/$Ag_2ZrO_3$ nanocomposite are analogous to those of pure g-$C_3N_4$ and $Ag_2ZrO_3$, and there are no other distinguished peaks noted in the recorded XRD pattern (Fig. 2). Further, a peak emerges about 27°, in the synthesized composite which may be related to the hybridization between g-$C_3N_4$ and $Ag_2ZrO_3$.

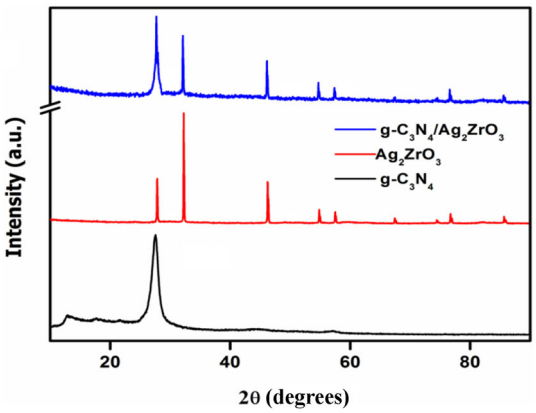


**Fig. 2** Powder XRD pattern of g-$C_3N_4$, $Ag_2ZrO_3$, and g-$C_3N_4$/$Ag_2ZrO_3$

UV–Vis DRS spectra of g-$C_3N_4$, $Ag_2ZrO_3$, and g-$C_3N_4$/$Ag_2ZrO_3$ are displayed in Fig. 3a. To find the band-gap energy of the materials, the following Tauc Eq. (1) was used [36, 44].

$$\alpha h\nu = A\left(h\nu - E_g\right)^{n/2}, \tag{1}$$

where $\alpha$, $h$, $\nu$, $A$, and $E_g$ are the absorption coefficient of the nanomaterial, Planck's constant, frequency of light, proportionality constant, and band-gap energy of the materials, respectively. The type of transition in the material could be determined from its n values ($n$ = 1 and 4, respectively, for direct and indirect transitions). By plotting $(\alpha h\nu)^2$ vs. $h\nu$ and extrapolating the graph to the x-axis as in Fig. 3b, $E_g$ values for the g-$C_3N_4$, $Ag_2ZrO_3$, and g-$C_3N_4$/$Ag_2ZrO_3$ were obtained as 2.73, 2.33, and 2.22 eV, respectively. The observation of reduction in the $E_g$ values clearly shows the efficient creation of tight chemically bounded interfaces between the g-$C_3N_4$ and $Ag_2ZrO_3$ phases in g-$C_3N_4$/$Ag_2ZrO_3$ nanocomposite.

The FE-SEM images for the g-$C_3N_4$, $Ag_2ZrO_3$, and g-$C_3N_4$/$Ag_2ZrO_3$ are given in Fig. 4a–c. g-$C_3N_4$ appears as multiple wrinkled-layer stack, whereas $Ag_2ZrO_3$ and g-$C_3N_4$/$Ag_2ZrO_3$ seem as regular granules. Furthermore, it is also noted that spherical-shaped $Ag_2ZrO_3$ nanoparticles were evenly anchored and distributed over the surface of graphitic carbon nitride.

TEM image of Fig. 5a g-$C_3N_4$ shows smooth sheet-like structures with sharp edges and crystal clear lattice fringes. TEM image of g-$C_3N_4$/$Ag_2ZrO_3$ nanocomposite in Fig. 5b shows the homogeneous

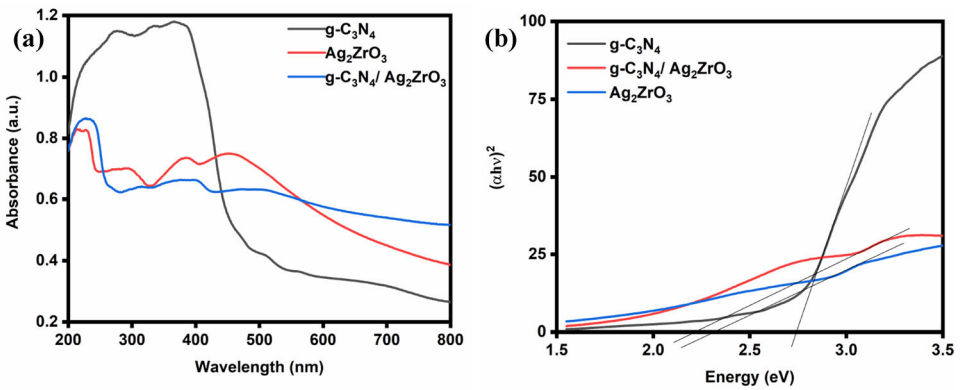


**Fig. 3** UV–Vis DRS spectra (**a**) and Tauc plot (**b**), for g-$C_3N_4$, $Ag_2ZrO_3$, and g-$C_3N_4$/$Ag_2ZrO_3$

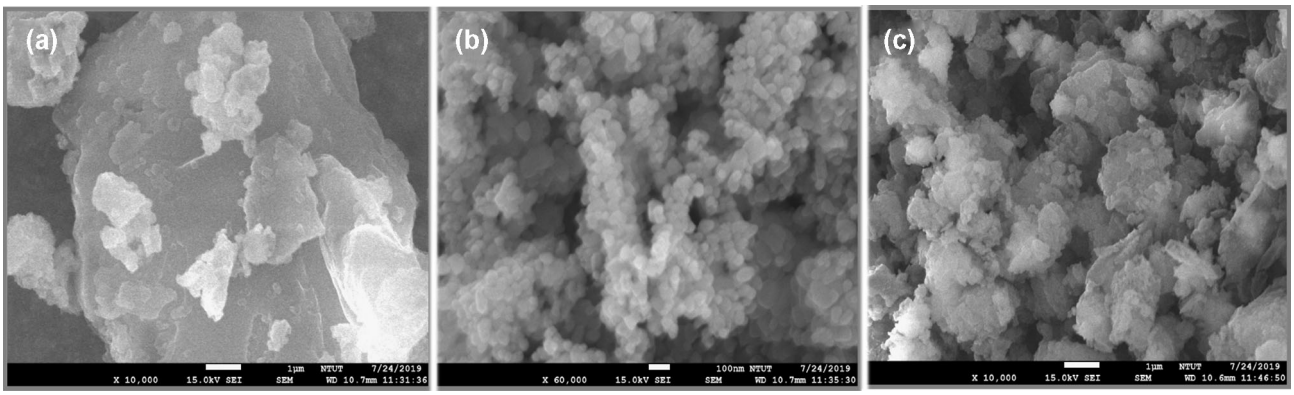


**Fig. 4** FE-SEM images of (**a**) g-$C_3N_4$, (**b**) $Ag_2ZrO_3$ and (**c**) g-$C_3N_4$/$Ag_2ZrO_3$

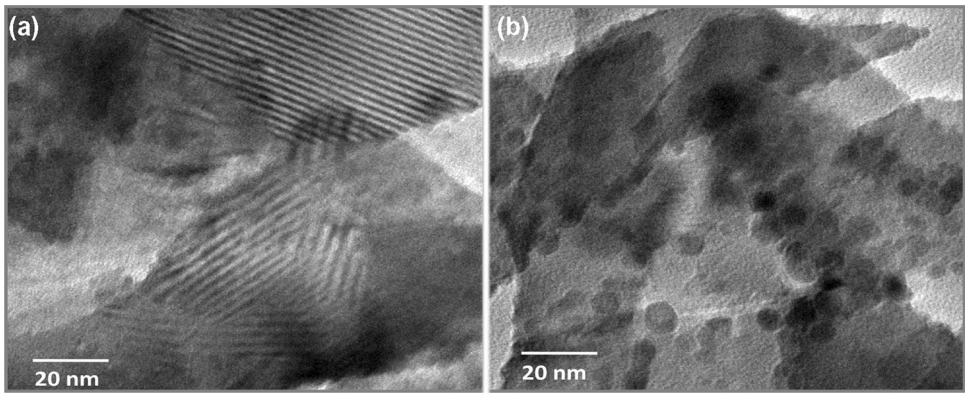


**Fig. 5** TEM images of (**a**) g-$C_3N_4$ and (**b**) g-$C_3N_4$/$Ag_2ZrO_3$

dispersion of the spherical $Ag_2ZrO_3$ nanoparticles on the entire surface of g-$C_3N_4$ nanosheets.

The specific surface area and pore size of g-$C_3N_4$, $Ag_2ZrO_3$, and g-$C_3N_4$/$Ag_2ZrO_3$ were studied using nitrogen adsorption–desorption analysis (Fig. 6). The Brunauer–Emmett–Teller (BET)-specific surface area of the g-$C_3N_4$/$Ag_2ZrO_3$ was measured to be about 136 $m^2/g$ which is considerably higher than g-$C_3N_4$ (12.41 $m^2/g$) and $Ag_2ZrO_3$ (31.19 $m^2/g$). The higher surface area may be due to good interaction between their counter parts leading to the formation of the aggregated pores among them. This provided more reaction sites, which in turn enhanced the electron–hole charge separation causing improvement in the sensor efficiency as compared to g-$C_3N_4$ and $Ag_2ZrO_3$. Further, pore size is also decreased for g-$C_3N_4$/$Ag_2ZrO_3$ (17.99 Å) compared to g-$C_3N_4$ (76.92 Å) and $Ag_2ZrO_3$ (28.18 Å).

## 3.2 Gas sensor studies

Preliminarily, gas sensor studies were tested for the g-$C_3N_4$, $Ag_2ZrO_3$, and g-$C_3N_4$/$Ag_2ZrO_3$ against 50 ppm concentration of six different gases namely n-butanol, isopropanol, methanol, xylene, toluene, and ethanol at room temperature. Depends on the variation in the chemiresistance behavior of g-$C_3N_4$, $Ag_2ZrO_3$, and g-$C_3N_4$/$Ag_2ZrO_3$ in the absence and presence of six different gases, the following parameters have been calculated by using Eqs. (2) and (3) [35, 36].

$$\text{Gas sensor response } (\%) = \left[\left(R_a - R_g\right)/R_a\right] \times 100, \tag{2}$$

$$\text{Gas sensor response (in times)} = R_a/R_g, \tag{3}$$

where $R_a$ and $R_g$ are the resistance value of the sensors in air and test gas, respectively.

By monitoring the alteration in the chemiresistance of the sensor in the presence of air and exposed gas, sensor response (%) for the chosen nanomaterials against six different gases was plotted in Fig. 7, and it shows that all the g-$C_3N_4$, $Ag_2ZrO_3$, and g-$C_3N_4$/$Ag_2ZrO_3$-based sensors more selectively distinguish ethanol gas in comparison to other gases. Particularly, g-$C_3N_4$ and $Ag_2ZrO_3$ display moderate sensor response values of 15.1% and 24.5% against ethanol

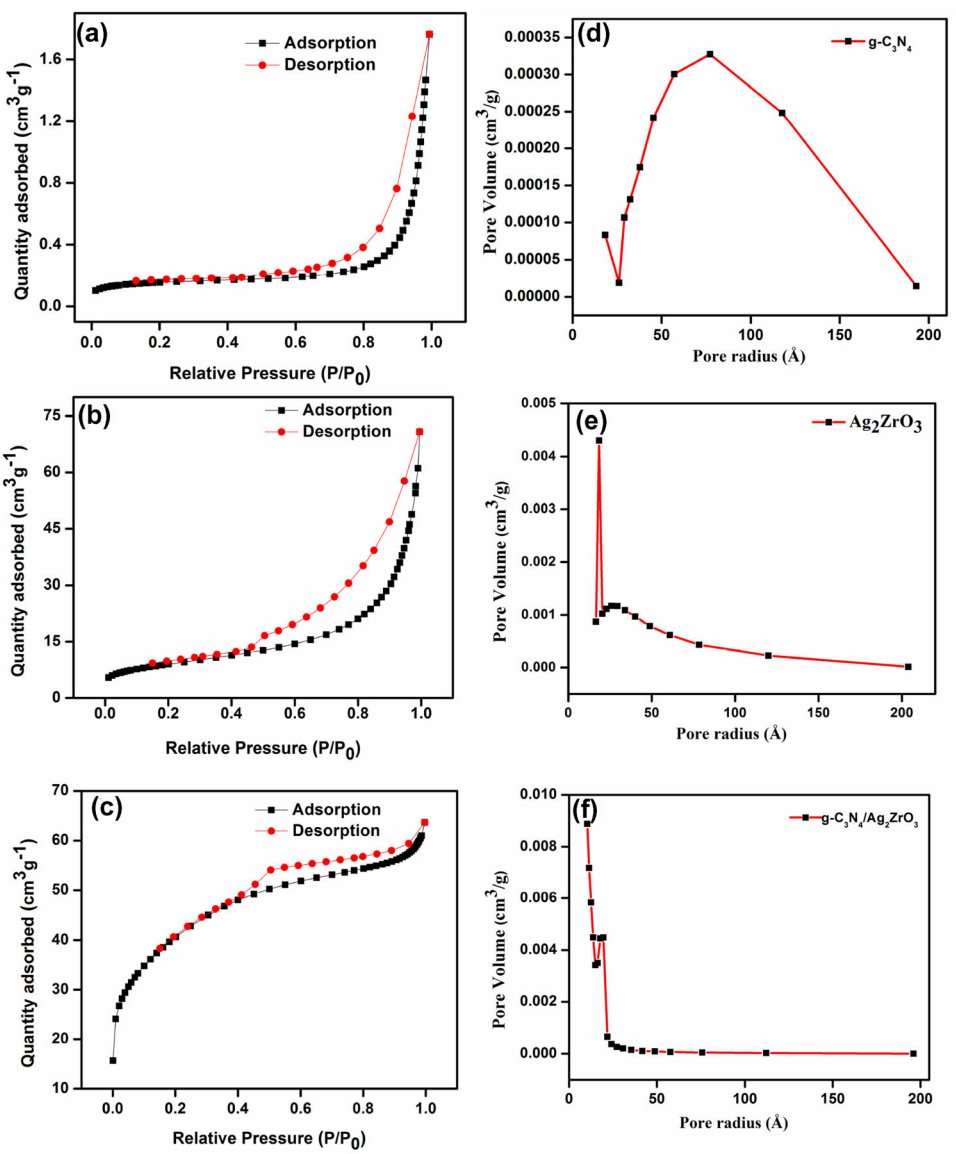


**Fig. 6** BET surface area of (**a**) g-$C_3N_4$, (**b**) $Ag_2ZrO_3$ and (**c**) g-$C_3N_4$/$Ag_2ZrO_3$; Pore size distribution curve of (**d**) g-$C_3N_4$, (**e**) $Ag_2ZrO_3$ and (**f**) g-$C_3N_4$/$Ag_2ZrO_3$

gas, respectively, while g-$C_3N_4$/$Ag_2ZrO_3$ shows highest sensor response value of 53.1% for ethanol compare to other gases, possibly due to the involvement of cooperative effect of g-$C_3N_4$ and $Ag_2ZrO_3$ in the gas-sensing mechanism. With reference to literature, there are a limited number of reports only obtainable for the room-temperature-operatable ethanol gas sensors. It could be seen from Table 1 that the present g-$C_3N_4$/$Ag_2ZrO_3$-based ethanol sensor shows a significant sensor response value even at room temperature.

To explain gas-sensing mechanism of investigated nanomaterials, involvement of gas adsorption-induced charge transfer could be utilized. It is well-known fact that the adsorption of molecular oxygen species on the surface of metal oxide-based gas sensor occurs upon exposing to air [17, 18, 21, 49]. The adsorbed oxygen species obtain electrons from the conduction band of g-$C_3N_4$/$Ag_2ZrO_3$ and become as chemisorbed ions ($O_2^-$, $O^-$, and $O^{2-}$) due to the high electron affinity of oxygen, through the Eqs. (4–7). Thus, depletion layer is produced on the outer surface of the sensing layer due to the decrease in the electron density by chemisorbed species [13, 20, 21, 50, 51]. According to Eqs. (8–13), the reducing gas molecules like ethanol adsorb on the surface of the sensor and undergo reaction with the chemisorbed oxygen ions resulting liberation of

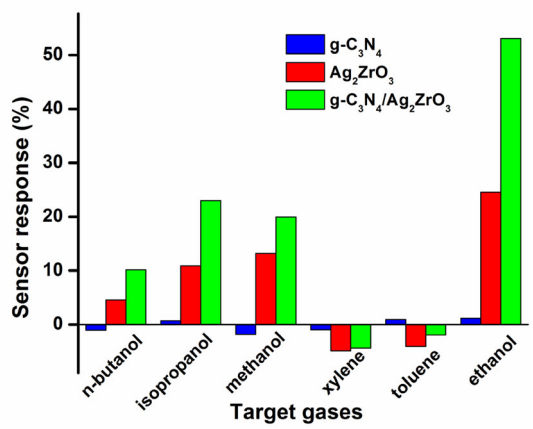


**Fig. 7** Sensor responses (%) of g-$C_3N_4$, $Ag_2ZrO_3$, and g-$C_3N_4$/$Ag_2ZrO_3$ against 50 ppm concentration of six different gases such as *n*-butanol, isopropanol, methanol, xylene, toluene, and ethanol at room temperature

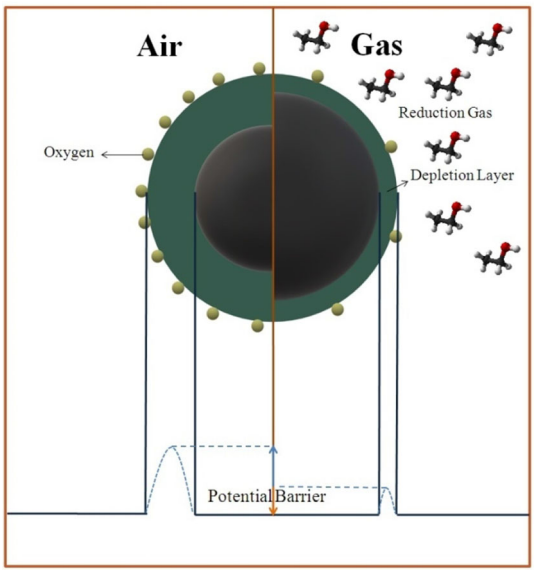


**Fig. 8** Mechanism of gas sensing by the semiconducting metal oxide through formation of depletion layer

electrons back to the surface of the sensing layer. The observed high selectivity of g-$C_3N_4$/$Ag_2ZrO_3$ against ethanol gas may be dependent on the structural and electronic properties of the prepared nanomaterials. As shown in Fig. 8, the gas-sensing mechanism is stoutly reliant on the accessibility of active sites on the surface of gas sensor.

(i) In the presence of air,

$$O_2(gas) \rightarrow O_2(ads), \tag{4}$$

$$O_2(ads) + e^- \rightarrow O_2^-, \tag{5}$$

$$O_2^- + e^- \rightarrow O^-, \tag{6}$$

$$O^- + e^- \rightarrow O_2^-. \tag{7}$$

(ii) In the presence of gas,

$$C_4H_{10}O + 6O_2^-(gas) \rightarrow 4CO_2 + 5H_20 + 12e^-, \tag{8}$$

$$CH_3CH(OH)CH_3(gas) + 9O^-(ads) \rightarrow 3CO_2 + 4H_2O + 9e^-, \tag{9}$$

$$CH_3OH(gas) + O_2^-(ads) \rightarrow HCOOH + H_2O + e^-, \tag{10}$$

$$C_6H_4CH_3CH_3(gas) + 2O^-(ads) \rightarrow C_6H_4CH_3CHO + H_2O + e^-, \tag{11}$$

$$C_7H_8(gas) + 9O_2^-(ads) \rightarrow 7CO_2 + 4H_2O + 9e^-, \tag{12}$$

**Table 1** Comparison of ethanol gas sensor performance for some g-$C_3N_4$-based nanomaterials

| S. no | Sensing material | Conc. in ppm | Operating temperature (°C) | Response |
|---|---|---|---|---|
| 1 | $SnO_2$/g-$C_3N_4$ | 500 | 300 | 240 [33][b] |
| 2 | $SnO_2$ | 100 | 225 | 17.3 [45][a] |
| 3 | α- $Fe_2O_3$/ g-$C_3N_4$ | 100 | 340 | 7.76 [46][a] |
| 4 | ZnO | 350 | 300 | 37 [47][a] |
| 5 | g-$C_3N_4$/ZnO | 350 | 100 | 15.8 [34][a] |
| 6 | Pt/ZnO/g-$C_3N_4$ | 250 | 50 | 66 [48][a] |
| 8 | g-$C_3N_4$ | 50 | RT | 15.1 (Present work)[a] |
| 9 | $Ag_2ZrO_3$ | 50 | RT | 24.5 (Present work)[a] |
| 10 | g-$C_3N_4$/$Ag_2ZrO_3$ | 50 | RT | 53.1 (Present work)[a] |

[a]Response (%) = $[(R_a–R_g)/R_a] \times 100$

[b]Response (in times) = $R_a/R_g$

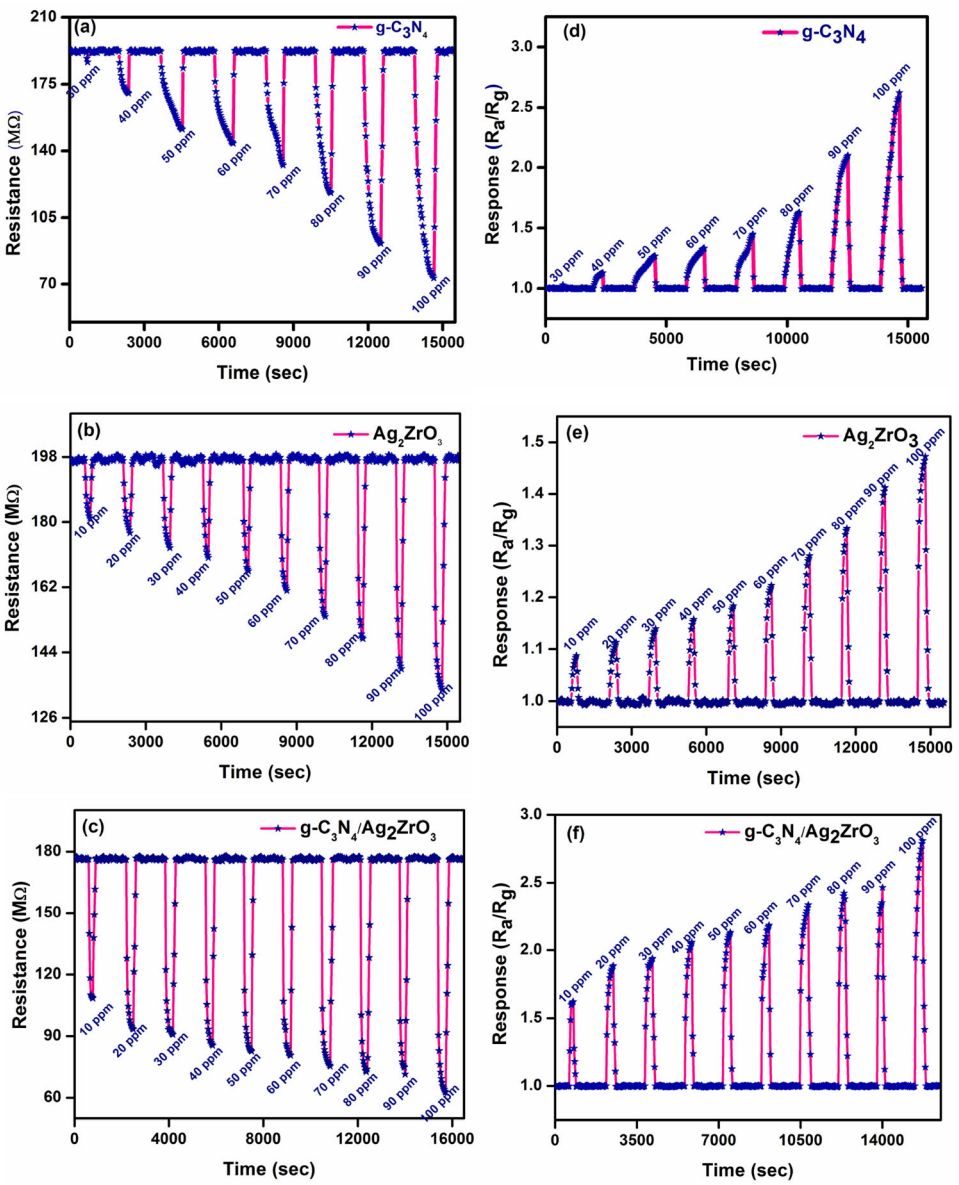


**Fig. 9** Resistance plots (**a**–**c**) and response plots (**d**–**f**) of g-$C_3N_4$, $Ag_2ZrO_3$, and g-$C_3N_4$/$Ag_2ZrO_3$ for sensing the ethanol gas at room temperature

$$C_2H_5OH(gas) + 3O_2^-(ads) \rightarrow 2CO_2 + 3H_2O + 3e^-. \quad (13)$$

Among the different gases examined, the nanomaterials g-$C_3N_4$, $Ag_2ZrO_3$, and g-$C_3N_4$/$Ag_2ZrO_3$ have shown high sensitivity against the ethanol gas and, thus, the gas sensor studies were detailed against ethanol gas in the concentration range of 1–1000 ppm by examining alteration in the resistance value upon alternative exposure of air and ethanol gas. As given in Fig. 9a–c, the resistance value of g-$C_3N_4$/$Ag_2ZrO_3$ is stable in atmospheric air and gets decreased abruptly upon introduction of ethanol gas and then attains a stable value. Further, the initial resistance value of sensor is yet again relapsed upon expelling the ethanol gas from the chamber, for the all concentrations investigated.

The fabricated g-$C_3N_4$/$Ag_2ZrO_3$-based gas sensor has considerable reversibility for the sensing the ethanol gas upon a rapid switching between air and gas. By using Eq. (3), sensor response values for the g-$C_3N_4$, $Ag_2ZrO_3$, and g-$C_3N_4$/$Ag_2ZrO_3$ were calculated, and the values were plotted against time for the all concentrations investigated (Fig. 9d–f). Upon increasing the concentration of ethanol (1–1000 ppm), g-$C_3N_4$/$Ag_2ZrO_3$ exposed a linear enhancement in the sensor response, whereas g-$C_3N_4$ and $Ag_2ZrO_3$ showed only moderate sensor responses.

The enhancement in the ethanol gas-sensing performance of g-$C_3N_4$/$Ag_2ZrO_3$ can be explained based on the creation of potential active sites in the g-$C_3N_4$/$Ag_2ZrO_3$ sensor with reference to both g-$C_3N_4$ and $Ag_2ZrO_3$ sensors. Further chemisorbed oxygen anions may liberate trapped electrons back to $Ag_2ZrO_3$, and extra electrons may go into $Ag_2ZrO_3$ from g-$C_3N_4$, which may lead to cooperatively improve the detection of ethanol gas upon exposure of ethanol gas on g-$C_3N_4$/$Ag_2ZrO_3$ sensor. In addition, there is also possibility of the oxidation of ethanol molecules by g-$C_3N_4$ through the formation of hydroxyl species. The enhanced response of g-$C_3N_4$/$Ag_2ZrO_3$ may lead to stimulate the electron exchange between the sensor material and target gas. Furthermore, the presence of Ag in the $Ag_2ZrO_3$ may enhance the creation of huge amount of active reaction sites on the surface of g-$C_3N_4$. Then, the width of the electron depletion layer is broadened as a result of the adsorbed oxygen molecules, which gain electrons rapidly to generate oxygen ions by means of catalytic action of Ag. Hence, there may be possible to create more number of reaction sites between ethanol gas molecules and chemisorbed oxygen ions at the sensor surface, which leads to the release of electrons back to the surface of the sensing layer.

It could be noted from the response graphs in Fig. 9d–f that the response of g-$C_3N_4$/$Ag_2ZrO_3$ sensor enhances with the increase of ethanol concentration and its response is relatively higher for g-$C_3N_4$/$Ag_2ZrO_3$ than pure g-$C_3N_4$ and $Ag_2ZrO_3$. Then, the sensitivity of g-$C_3N_4$, $Ag_2ZrO_3$, and g-$C_3N_4$/$Ag_2ZrO_3$ was calculated by making a plot between concentration of ethanol (x) and response (y). g-$C_3N_4$/$Ag_2ZrO_3$ displayed high sensitivity value (1.538 $ppm^{-1}$) in comparision with both g-$C_3N_4$ (1.016 $ppm^{-1}$) and $Ag_2ZrO_3$ (0.356 $ppm^{-1}$), and the composite material also has good linearity in gas sensor behavior which is very much needed for the quantitative measurement of ethanol gas (Fig. 10).

The repeatability of the gas sensor response of g-$C_3N_4$/$Ag_2ZrO_3$ was recorded for five successive response/recovery cycles under the concentration of 50 ppm ethanol gas at room temperature. The observed profile in Fig. 11a displays the similarity and steady repeatability of g-$C_3N_4$/$Ag_2ZrO_3$ for ethanol gas sensing. The long-term stability of the sensor for over time is an important aspect for its economical usage. The resistance of g-$C_3N_4$/$Ag_2ZrO_3$ sensor for the detection of 50 ppm concentration of

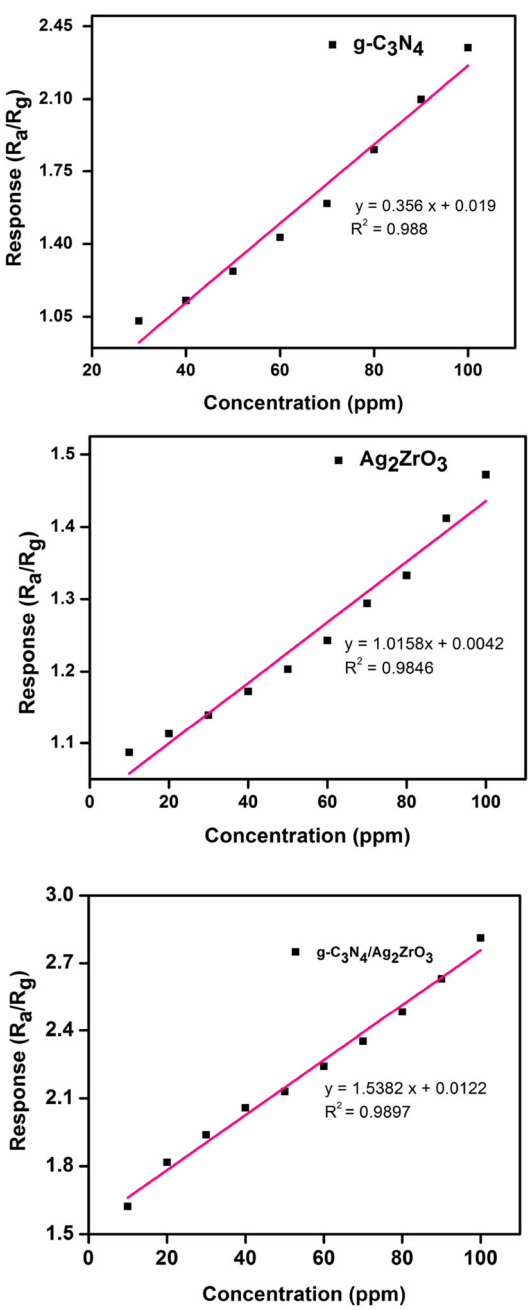


**Fig. 10** Sensitivity graphs of g-$C_3N_4$, $Ag_2ZrO_3$ and g-$C_3N_4$/$Ag_2ZrO_3$-based gas sensors in the concentration range of 10–100 ppm of ethanol

ethanol gas over a time of 24 days is shown in Fig. 11 (b). The obtained results show that g-$C_3N_4$/$Ag_2ZrO_3$ sensor has good repeatability and showed nearly constant resistance values as needed for excellent long-term stability. The stability of resistance value of g-$C_3N_4$/$Ag_2ZrO_3$ in the absence and presence of ethanol gas at 50 ppm is shown in Fig. 11c, and the

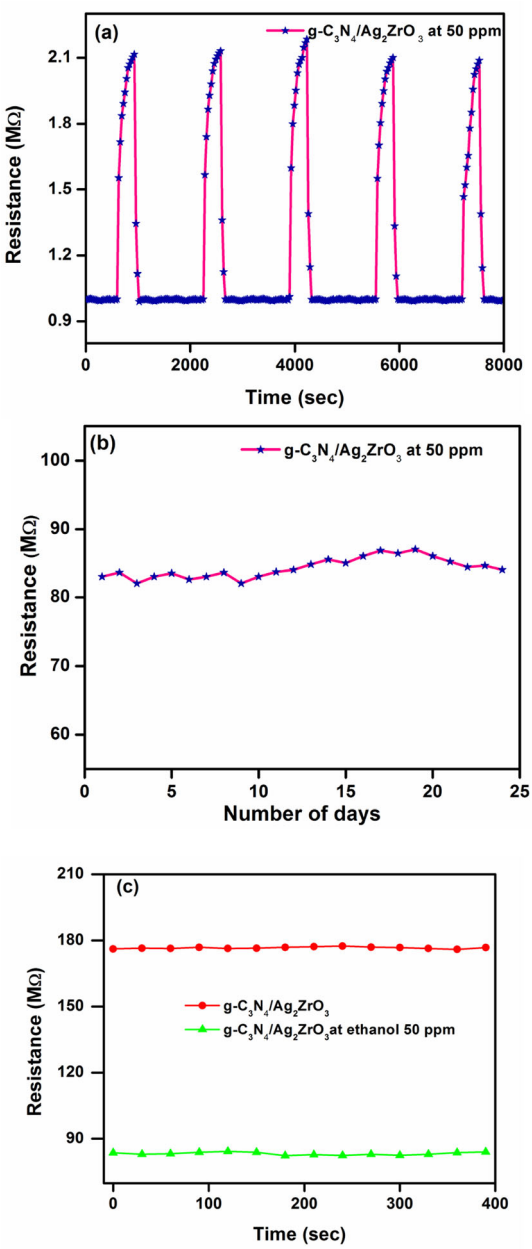


**Fig. 11** (**a**) Repeatability in the sensor response of g-$C_3N_4$/$Ag_2ZrO_3$ for the five successive cycles at 50 ppm of ethanol gas; (**b**) Long-term reproducibility of resistance of g-$C_3N_4$/$Ag_2ZrO_3$ in the presence of ethanol gas at 50 ppm; (**c**) Stability of the resistance of g-$C_3N_4$/$Ag_2ZrO_3$ in air and g-$C_3N_4$/$Ag_2ZrO_3$ at 50 ppm of ethanol

results show the almost stable resistance value for ethanol gas sensing.

## 4 Conclusion

In this investigation, g-$C_3N_4$, $Ag_2ZrO_3$, and g-$C_3N_4$/$Ag_2ZrO_3$ was synthesized and characterized by using UV-DRS, XRD, FE-SEM, TEM, and BET. Gas sensor studies for the g-$C_3N_4$, $Ag_2ZrO_3$, and g-$C_3N_4$/$Ag_2ZrO_3$ were analyzed against 50 ppm concentration of six different gases namely against ethanol gas compare to n-butanol, isopropanol, methanol, xylene, and toluene gases at room temperature. Among the six different gases, g-$C_3N_4$/$Ag_2ZrO_3$ has shown high sensitivity against ethanol gas, and hence, the gas sensor studies were detailed for ethanol gas sensor. The g-$C_3N_4$ and $Ag_2ZrO_3$ showed moderate relative sensor response value of 15.1% and 24.5% against ethanol, while g-$C_3N_4$/$Ag_2ZrO_3$ showed the highest relative sensor response value of 53.1% for ethanol compared to other gases conceivably due to involvement of cooperative effect of g-$C_3N_4$ and $Ag_2ZrO_3$. Further, g-$C_3N_4$/$Ag_2ZrO_3$ gas sensor showed excellent repeatability, quick response/recovery, and good stability for the detection of ethanol gas. Thus, this kind of modification of chemiresistive semiconductor metal oxide nanocomposite will afford room-temperature-operatable high-performance gas sensors in near future.

## Acknowledgements

Dr. S. Kalaiselvam expresses sincere gratitude to the Science and Engineering Research Board (SERB), Department of Science and Technology (DST), for supporting the research work under EEQ [SERB Sanction Order No. EEQ/2018/000694]; Dr. S. Veeralakshmi thanks DST-Women Scientist Scheme-A (SR/WOS-A/CS-40/2018 (G)); Dr. S. Nehru acknowledges DST-SERB (EEQ/2018/001402) and RUSA 2.0, University of Madras for providing financial support.

## Author contributions

All authors contributed to the study conception and design. Material preparation, data collection, and analysis were performed by SD, SV, and SN. The first draft of the manuscript was written by SD and SV.

Nehru and MS edited the entire draft. SK supervised the whole work and edited the manuscript. All authors read and approved the final manuscript.

## Funding

Dr. S. Kalaiselvam expresses sincere gratitude to the Science and Engineering Research Board (SERB), Department of Science and Technology (DST), for supporting the research work under EEQ [SERB Sanction Order No. EEQ/2018/000694]; Dr. S. Veeralakshmi thanks DST-Women Scientist Scheme-A (SR/WOS-A/CS-40/2018 (G)); Dr. S. Nehru acknowledges DST-SERB (EEQ/2018/001402) and RUSA 2.0, University of Madras for providing financial support.

## Data availability

The datasets generated during the current study are available from the corresponding author on reasonable request.

## Declarations

**Conflict of interest** The authors declare no competing financial interest. The authors declare that they have no known competing financial interests or personal relationships that could have appeared to influence the work reported in this paper.

## References

1. R.A. Dagle, A.D. Winkelman, K.K. Ramasamy, V. Lebarbier Dagle, R.S. Weber, Ethanol as a renewable building block for fuels and chemicals. Ind. Eng. Chem. Res. **59**(11), 4843–4853 (2020)
2. B. Le Dare, T. Gicquel, Therapeutic applications of ethanol: A review. J. Pharm. Pharm. Sci. **22**, 525–535 (2019)
3. B. Le Daré, V. Lagente, T. Gicquel, Ethanol and its metabolites: update on toxicity, benefits, and focus on immunomodulatory effects. Drug Metab. Rev. **51**(4), 545–561 (2019)
4. Y. Tizabi, B. Getachew, M.A. Collins. Ethanol neurotoxicity. Handbook of Neurotoxicity. 1–23 (2021)
5. W. Tian, X. Liu, W. Yu, Research progress of gas sensor based on graphene and its derivatives: a review. Appl. Sci. **8**(7), 1118 (2018)
6. M. Righettoni, A. Amann, S.E. Pratsinis, Breath analysis by nanostructured metal oxides as chemo-resistive gas sensors. Mater. Today **18**(3), 163–171 (2015)
7. H. Tai, S. Wang, Z. Duan, Y. Jiang, Evolution of breath analysis based on humidity and gas sensors: potential and challenges. Sensors Actuators B: Chem. **318**, 128104 (2020)
8. P.R. Galassetti, B. Novak, D. Nemet, C. Rose-Gottron, D.M. Cooper, S. Meinardi et al., Breath ethanol and acetone as indicators of serum glucose levels: an initial report. Diabetes Technol. Ther. **7**(1), 115–123 (2005)
9. P. Srinivasan, M. Ezhilan, A.J. Kulandaisamy, K.J. Babu, J.B.B. Rayappan, Room temperature chemiresistive gas sensors: challenges and strategies—a mini review. J. Mater. Sci.: Mater. Electron. **30**(17), 15825–15847 (2019)
10. J. Zhang, X. Liu, G. Neri, N. Pinna, Nanostructured materials for room-temperature gas sensors. Adv. Mater. **28**(5), 795–831 (2016)
11. N. Joshi, T. Hayasaka, Y. Liu, H. Liu, O.N. Oliveira, L. Lin, A review on chemiresistive room temperature gas sensors based on metal oxide nanostructures, graphene and 2D transition metal dichalcogenides. Microchim. Acta **185**(4), 1–16 (2018)
12. L. Guatwei, T. Xian-ju, C. Choongyew, A. Gaiktin, A.B.M. Zailani, Development of tungsten oxide based gas sensor for ethanol vapor detection. J. Mater. Sci. Eng. **5**(3), 271 (2011)
13. A.V. Raghu, K.K. Karuppanan, J. Nampoothiri, B. Pullithadathil, Wearable, flexible ethanol gas sensor based on $TiO_2$ nanoparticles-grafted 2D-titanium carbide nanosheets. ACS Appl. Nano Mater. **2**(3), 1152–1163 (2019)
14. Q. Ding, J. Li, Y. Wang, B. Wang, W. Zhu, X. OuYang et al., Enhanced sensing performance of $TiO_2$/Ag2V4O11 nanoheterostructures to ethanol gas. J Alloys Compd. **811**, 151958 (2019)
15. S. Park, S. Kim, G.-J. Sun, C. Lee, Synthesis, structure, and ethanol gas sensing properties of In2O3 nanorods decorated with Bi2O3 nanoparticles. ACS Appl. Mater. Interfaces. **7**(15), 8138–8146 (2015)
16. T.T. Nguyen, H.-N. Choi, M.J. Ahemad, D. Van Dao, I.-H. Lee, Y.-T. Yu, Hydrothermal synthesis of $In_2O_3$ nanocubes for highly responsive and selective ethanol gas sensing. J. Alloys Comps. **820**, 153133 (2020)
17. Y. Li, S. Song, L.-B. Zhang, X.-X. Lian, L.-X. Shan, Q.-J. Zhou, Fabrication of hollow porous ZnO@ ZnS heterostructures via hydrothermal method and enhanced gas-sensing performance for ethanol. J. Alloys Compd. **855**, 157430 (2021)
18. P. Wang, S.-Z. Wang, Y.-R. Kang, Z.-S. Sun, X.-D. Wang, Y. Meng et al., Cauliflower-shaped $Bi_2O_3$–ZnO heterojunction with superior sensing performance towards ethanol. J. Alloys Compd. **854**, 157152 (2021)

19. F. Xu, C. Zhou, H.-P. Ho, A rule for operation temperature selection of a conductometric VOC gas sensor based on ZnO nanotetrapods. J. Alloys Compd. **858**, 158294 (2021)
20. W. Tan, Q. Yu, X. Ruan, X. Huang, Design of $SnO_2$-based highly sensitive ethanol gas sensor based on quasi molecular-cluster imprinting mechanism. Sens. Actuators, B Chem. **212**, 47–54 (2015)
21. L. Zhang, R. Tong, W. Ge, R. Guo, S.E. Shirsath, J. Zhu, Facile one-step hydrothermal synthesis of $SnO_2$ microspheres with oxygen vacancies for superior ethanol sensor. J. Alloys Compd. **814**, 152266 (2020)
22. C. Liu, Q. Kuang, Z. Xie, L. Zheng, The effect of noble metal (Au, Pd and Pt) nanoparticles on the gas sensing performance of $SnO_2$-based sensors: a case study on the 221 high-index faceted $SnO_2$ octahedra. CrystEngComm **17**(33), 6308–6313 (2015)
23. A. Mirzaei, J.-H. Lee, S.M. Majhi, M. Weber, M. Bechelany, H.W. Kim et al., Resistive gas sensors based on metal-oxide nanowires. J. Appl. Phys. **126**(24), 241102 (2019)
24. S. Park, G.-J. Sun, C. Jin, H.W. Kim, S. Lee, C. Lee, Synergistic effects of a combination of Cr2O3-functionalization and UV-irradiation techniques on the ethanol gas sensing performance of ZnO nanorod gas sensors. ACS Appl. Mater. Interfaces. **8**(4), 2805–2811 (2016)
25. J. Liu, T. Wang, B. Wang, P. Sun, Q. Yang, X. Liang et al., Highly sensitive and low detection limit of ethanol gas sensor based on hollow ZnO/$SnO_2$ spheres composite material. Sens. Actuators, B Chem. **245**, 551–559 (2017)
26. L. Zhu, Y. Li, W. Zeng, Hydrothermal synthesis of hierarchical flower-like ZnO nanostructure and its enhanced ethanol gas-sensing properties. Appl. Surf. Sci. **427**, 281–287 (2018)
27. Y. Qin, G. Fan, K. Liu, M. Hu, Vanadium pentoxide hierarchical structure networks for high performance ethanol gas sensor with dual working temperature characteristic. Sens. Actuators, B Chem. **190**, 141–148 (2014)
28. W. Guo, Hollow and porous ZnSnO3 gas sensor for ethanol gas detection. J. Electrochem. Soc. **163**(5), B131 (2016)
29. M. Tiemann, Porous metal oxides as gas sensors. Chem. A Eur. J. **13**(30), 8376–8388 (2007)
30. X.-F. Wang, X.-Z. Song, K.-M. Sun, L. Cheng, W. Ma, MOFs-derived porous nanomaterials for gas sensing. Polyhedron **152**, 155–163 (2018)
31. G. Dong, Y. Zhang, Q. Pan, J. Qiu, A fantastic graphitic carbon nitride (g-C3N4) material: electronic structure, photocatalytic and photoelectronic properties. J. Photochem. Photobiol. C **20**, 33–50 (2014)
32. P. Srinivasan, S. Samanta, A. Krishnakumar, J.B.B. Rayappan, K. Kailasam, Insights into g-C3N4 as chemi-resistive gas sensors towards VOCs and humidity-A review on state-of-the-art and recent advancements. J. Mater. Chem. A. (2021). https://doi.org/10.1039/D0TA12500H
33. J. Cao, C. Qin, Y. Wang, H. Zhang, B. Zhang, Y. Gong et al., Synthesis of $gC_3$ $N_4$ nanosheet modified $SnO_2$ composites with improved performance for ethanol gas sensing. RSC Adv. **7**(41), 25504–25511 (2017)
34. J. Cao, Y. Gong, Y. Wang, B. Zhang, H. Zhang, G. Sun et al., Cocoon-like ZnO decorated graphitic carbon nitride nanocomposite: Hydrothermal synthesis and ethanol gas sensing application. Mater. Lett. **198**, 76–80 (2017)
35. S.S. David, S. Veeralakshmi, J. Sandhya, S. Nehru, S. Kalaiselvam, Room temperature operatable high sensitive toluene gas sensor using chemiresistive Ag/$Bi_2O_3$ nanocomposite. Sensors Actuators B Chem. **320**, 128410 (2020)
36. S.S.D.S. David, S. Veeralakshmi, S. Nehru, S. Kalaiselvam, A highly sensitive, selective and room temperature operatable formaldehyde gas sensor using chemiresistive g-C3N4/ZnO. Mater. Adv. (2020). https://doi.org/10.1039/D0MA00529K
37. S.K. Warkhade, R.S. Das, G. Gaikwad, U.R. Pratap, S.P. Zodape, A.V. Wankhade, A facile microwave assisted fabrication of nano Ag2ZrO3: an efficient visible light harvesting photocatalyst. Environ. Progress Sustain. Energy **38**(3), e13071 (2019)
38. R.S. Das, S.K. Warkhade, A. Kumar, G. Gaikwad, A.V. Wankhade, Graphitic carbon nitride@ silver zirconate nanocomposite (gC3N4@ Ag2ZrO3): a Type-II heterojunction for an effective visible light photocatalysis and bacterial photo-inactivation. J. Alloys Compd. **846**, 155770 (2020)
39. P. Murugesan, S. Narayanan, M. Manickam, P.K. Murugesan, R. Subbiah, A direct Z-scheme plasmonic AgCl@ g-C3N4 heterojunction photocatalyst with superior visible light CO2 reduction in aqueous medium. Appl. Surf. Sci. **450**, 516–526 (2018)
40. D.J. Martin, K. Qiu, S.A. Shevlin, A.D. Handoko, X. Chen, Z. Guo et al., Highly efficient photocatalytic H2 evolution from water using visible light and structure-controlled graphitic carbon nitride. Angew. Chem. Int. Ed. **53**(35), 9240–9245 (2014)
41. S.R. Thakare, G. Gaikwad, N. Khati, A. Wankhade, Development of new, highly efficient and stable visible light active photocatalyst Ag2ZrO3 for methylene blue degradation. Catal. Commun. **62**, 39–43 (2015)
42. S.G. Ampian, X-ray and optical crystallographic data for Na2ZrO3. J. Am. Ceram. Soc. **51**(10), 607–608 (1968)
43. K. Yin, T. Wang, J. Zhang, A. Gao, M. Shao, The effects of gamma ray irradiation on the photocatalytic efficiency: a way to enhance the Lewis acid–base interaction between Ag2SnO3 and Congo Red. Mater. Lett. **113**, 17–19 (2013)

44. S. Veeralakshmi, S. Kalaiselvam, R. Murugan, P. Pandurangan, S. Nehru, S. Sakthinathan et al., An approach to develop high performance supercapacitor using Bi 2 O 3 based binary and ternary nanocomposites. J. Mater. Sci.: Mater. Electron. **31**(24), 22417–22426 (2020)
45. Y. Wang, C. Liu, L. Wang, J. Liu, B. Zhang, Y. Gao et al., Horseshoe-shaped SnO2 with annulus-like mesoporous for ethanol gas sensing application. Sens. Actuators, B Chem. **240**, 1321–1329 (2017)
46. J. Cao, C. Qin, Y. Wang, B. Zhang, Y. Gong, H. Zhang et al., Calcination method synthesis of SnO2/g-C3N4 composites for a high-performance ethanol gas sensing application. Nanomaterials **7**(5), 98 (2017)
47. M.R. Alenezi, A.S. Alshammari, K.I. Jayawardena, M.J. Beliatis, S.J. Henley, S. Silva, Role of the exposed polar facets in the performance of thermally and UV activated ZnO nanostructured gas sensors. J. Phys. Chem. C. **117**(34), 17850–17858 (2013)
48. H. Tian, H. Fan, J. Ma, Z. Liu, L. Ma, S. Lei et al., Pt-decorated zinc oxide nanorod arrays with graphitic carbon nitride nanosheets for highly efficient dual-functional gas sensing. J. Hazard. Mater. **341**, 102–111 (2018)
49. H.R. Yousefi, B. Hashemi, A. Mirzaei, H. Roshan, M.H. Sheikhi, Effect of Ag on the ZnO nanoparticles properties as an ethanol vapor sensor. Mater. Sci. Semicond. Process. **117**, 105172 (2020)
50. C. Dong, X. Liu, X. Xiao, S. Du, Y. Wang, Monodisperse ZnFe2O4 nanospheres synthesized by a nonaqueous route for a highly slective low-ppm-level toluene gas sensor. Sens. Actuators, B Chem. **239**, 1231–1236 (2017)
51. T. Tharsika, M. Thanihaichelvan, A. Haseeb, S.A. Akbar, Highly sensitive and selective ethanol sensor based on zno nanorod on SnO2 thin film fabricated by spray pyrolysis. Front. Mater. **6**, 122 (2019)